

General Disclaimer

One or more of the Following Statements may affect this Document

- This document has been reproduced from the best copy furnished by the organizational source. It is being released in the interest of making available as much information as possible.
- This document may contain data, which exceeds the sheet parameters. It was furnished in this condition by the organizational source and is the best copy available.
- This document may contain tone-on-tone or color graphs, charts and/or pictures, which have been reproduced in black and white.
- This document is paginated as submitted by the original source.
- Portions of this document are not fully legible due to the historical nature of some of the material. However, it is the best reproduction available from the original submission.

End-Wall Boundary Layer Measurements in a Two-Stage Fan

(NASA-TM-83409) END-WALL BOUNDARY LAYER
MEASUREMENTS IN A TWO-STAGE FAN (NASA) 24 P
HC A02/MF A01 CSCI 01A

N83-24470

Unclas
G3/02 C3649

Calvin L. Ball, Lonnie Reid,
and James F. Schmidt
Lewis Research Center
Cleveland, Ohio



Prepared for the
Propulsion Energetics Panel
Sixty-first AGARD Specialists' Meeting
sponsored by AGARD
Copenhagen, Denmark, June 1-3, 1983

ORIGINAL PAGE IS
OF POOR QUALITY

END-WALL, BOUNDARY LAYER MEASUREMENTS IN A TWO-STAGE FAN

Calvin L. Ball, Lonnie Reid, and James F. Schmidt
National Aeronautics and Space Administration
Lewis Research Center
21000 Brookpark Road
Cleveland, Ohio 44135
U.S.A.

SUMMARY

Detailed flow measurements made in the casing boundary layer of a two-stage transonic fan are summarized. These measurements were taken at stations upstream of the fan, between all blade rows, and downstream of the last blade row. At the design tip speed of 429 m/sec the fan achieved a peak efficiency of 0.846 at a pressure ratio of 2.471. The boundary layer data were obtained at three weight flows at the design speed: one near choke flow, one near peak efficiency, and one near stall. Conventional boundary layer parameters were calculated from the data measured at each measuring station for each of the three flows. A classical two-dimensional casing boundary layer was measured at the fan inlet and extended inward to approximately 15 percent of span. A highly three-dimensional boundary layer was measured at the exit of each blade row and extended inward to approximately 10 percent of span. The steep radial gradient of axial velocity noted at the exit of the rotors was reduced substantially as the flow passed through the stators. This reduced gradient is attributed to flow mixing. The amount of flow mixing was reflected in the radial redistribution of total temperature as the flow passed through the stators. The data also show overturning of the tip flow at the stator exits that is consistent with the expected effect of the secondary flow field. The blockage factors calculated from the measured data show an increase in blockage across the rotors and a decrease across the stators. For this fan the calculated blockages for the second stage were essentially the same as those for the first stage.

SYMBOLS

C_f	skin friction coefficient, eq. (B6)
C_p	specific heat at constant pressure, 1004 J/kg K
D	diffusion factor, eq. (A1)
H_c	axial compressible form factor, eq. (B4)
H_i	axial incompressible form factor, eq. (B5)
K	blockage allowance, $1 - K_b$
K_b	blockage factor, eq. (A11)
K_{des}	design blockage allowance, $K_2 + K_3$
K_{meas}	calculated blockage from measured data, $K_1 + K_2$
K_1	equivalent blockage allowance associated with design end-wall loss
K_2	design blockage to account for tempering of design end-wall loss gradient relative to actual (measured gradient)
K_3	blockage resulting from nonaxisymmetric flows, eq. (A12)
M	Mach number
N	rotative speed, rpm
P	total pressure, N/cm ²
p	static pressure, N/cm ²
Pr	Prandtl number, 0.71
R	universal gas constant
r	radius, cm
T	total temperature, K
t	static temperature, K
U	wheel speed, m/sec; boundary layer air velocity, m/sec

ORIGINAL DESIGN
OF POOR QUALITY

22-2

V	air velocity, m/sec
W	weight flow, kg/sec
W(y/δ)	eq. (B12)
y	boundary layer distance from wall
z	axial distance referenced from rotor-blade-hub leading edge, cm
φ	relative air angle (angle between air velocity and axial direction), deg
γ	ratio of specific heats
δ	ratio of rotor-inlet total pressure to standard pressure of 10.13 N/cm ² ; edge of boundary layer distance
δ*	displacement thickness, eq. (B3)
η	efficiency
θ	ratio of rotor-inlet total temperature to standard temperature of 288.2 K; momentum thickness, eq. (B2)
μ	dynamic viscosity
ρ	density
Π	eq. (B10)
σ	solidity; ratio of chord to spacing
φ	flow coefficient, eq. (A7)
ψ _p	head-rise coefficient, eq. (A6)
ψ _T	temperature-rise coefficient, eq. (A9)

Subscripts:

ad	adiabatic (temperature rise)
aw	adiabatic wall condition
b	boundary layer
des	design
e	edge-of-boundary-layer condition
h	hub
inv	inviscid flow
LE	blade leading edge
meas	measured quantity
p	polytropic
ref	reference temperature condition
TE	blade trailing edge
t	tip
w	wall condition
x	boundary layer axial direction
z	boundary layer tangential direction
θ	flow tangential direction
τ	shear
0	plenum condition

Superscripts:

- ' relative to blade
- average quantity

INTRODUCTION

The strong influence of end-wall flows on compressor performance is well recognized. The potential benefit of being able to model these flows in multistage axial-flow compressors is evident by the large number of researchers who have treated various aspects of the subject over the years. The results of some of this research are presented in references 1 to 13 and summarized by Hirsch and Denton in reference 14. This modeling effort has treated, in addition to what might be considered the more classical annulus end-wall boundary layer approach, the influence of the various secondary flows on both the through-flow and tangential-flow radial gradients. The secondary-flow effects that have been considered include the passage vortex, flows due to secondary stresses, corner vortices, leakage flows, and the migration of the blade surface boundary layers, which tend to accumulate in the end-wall regions. Koch and Smith in reference 15 present a method for calculating the design-point efficiency potential of a multistage compressor that is based to a large extent on modeling the end-wall flows. Adkins and Smith in reference 16 present an approximate method to account for spanwise mixing in design through-flow calculation procedure. The spanwise mixing that occurs in a multistage axial-flow compressor is recognized to have a strong influence on the extent of the apparent end-wall boundary layer and thus on energy addition and losses. The Adkins and Smith procedure takes into account main-stream non-free-vortex flows, end-wall boundary layers, blade-end clearances, blade-end shrouding, and blade-surface boundary layer and wake centrifugation on flow mixing.

The success of the various modeling efforts is highly dependent on adequate experimental data for developing, extending, and validating the various features of the end-wall flow models. The NASA Lewis Research Center has a strong interest in the modeling of the end-wall flows in turbomachinery and in the validation of these models. The objective of this study was to obtain detailed flow measurements in the casing boundary layer of a two-stage transonic fan in order to expand on the somewhat limited experimental data base available from high-speed, high-pressure-ratio multistage fans and compressors for use in modeling and code verification.

The aerodynamic design along with the overall and blade-element performance of this fan is presented in reference 17. Data from this fan were used as a test case by the AGARD Propulsion and Energetics Panel, Working Group 12, for through-flow calculations in axial turbomachines. The results of that effort are presented in reference 14.

The flow measurements made in the casing boundary layer of this fan are presented in detail in reference 18 in both tabular and graphical forms. The data presented herein include the radial distributions of various flow parameters along with calculated boundary layer parameters based on the flow measurements. Data are presented for stations upstream of the fan, between all blade rows, and downstream of the last blade row for three weight flows at design speed: one near choke flow, one near peak efficiency, and one near stall.

DeRuyck and Hirsch of the Department of Fluid Mechanics, Vrije Universiteit-Brussel, Brussels, Belgium, calculated the boundary layer parameters for this fan by using their end-wall boundary layer prediction method for multistage axial-flow compressors (ref. 13). Their calculations used as input the aerodynamic design for the two-stage fan to include the running clearance for the blading and the flow points at which data were obtained. Comparisons between measured and predicted velocities in the end-wall region are presented by DeRuyck and Hirsch in reference 19.

The experimental data were obtained from tests conducted in the multistage compressor test facility at the Lewis Research Center, National Aeronautics and Space Administration, Cleveland, Ohio, U.S.A.

APPARATUS AND PROCEDURE

Two-Stage Fan

The overall design parameters for the two-stage fan are presented in table I. Flow blockage allowances are presented in table II. The flow path and axial locations of the measuring stations are shown in figure 1. The two-stage fan assembly is shown in figure 2. One obvious feature of this fan is the unusually large axial spacing between blade rows. It was configured this way to provide a fan representative of one designed to minimize blade-row interaction noise. Figure 2 shows the fan with casing treatment over the rotors. However, when taking the boundary layer data, solid inserts were installed over the rotor tips.

The fan was originally designed with a first-stage rotor having an aspect ratio of 2.9 and incorporated a part-span damper to eliminate potential aeroelastic problems. A number of damper configurations were tested in an attempt to maximize aerodynamic per-

ORIGINAL PAGE IS OF POOR QUALITY

22-4

formance and to maintain structural integrity. The results are reported in references 20 to 22. None of these configurations achieved the desired efficiency levels.

The first stage was redesigned to accommodate a rotor having an aspect ratio of 1.5, which eliminated the need for the dampers. The design and performance of the fan incorporating the low-aspect-ratio first-stage rotor are presented in reference 17. This modification resulted in a fan having excellent performance.

The fan with the low-aspect-ratio first-stage rotor was judged to be hub critical in terms of the blade elements that were controlling the stall line at the higher speeds. This judgment was in part based on the insensitivity (lack of movement) of the stall line to casing treatment. In addition the blade-element data indicated that the stall line was most likely being controlled by the flow in the hub region of the second stage (ref. 17).

The end-wall boundary layer measurements were obtained in the two-stage fan having the low-aspect-ratio first-stage rotor. Contrary to statements in reference 18, as noted earlier in this paper, circumferentially grooved casing treatment was not installed over both rotors during the boundary layer surveys. The rotor-tip running clearances were estimated to be 0.04 cm at design speed. The stator design incorporated a full chordwise platform at the tip, therefore eliminating the clearances.

The design of the low-aspect-ratio first-stage rotor considered an inlet-tip boundary layer total pressure based on unreported boundary layer survey data obtained with the configuration reported in reference 21. This resulted in the first-stage-rotor blading having leading-edge end-wall bends. The computer program used in the design and described in reference 23 was unable to handle the measured steep total-pressure gradient through the outer-wall boundary layer region. To alleviate this problem, the total-pressure distribution was tempered and combined with an end-wall blockage allowance of 0.01. It was expected that this modified accounting of the boundary layer would more closely align the blade with the flow entering the rotor at the tip and result in reduced losses. At the other stations in the two-stage fan, the hub and casing boundary layers were accounted for by increasing the flow loss in the end-wall regions and adding a blockage allowance. The blockage allowances at the tip were 0.013 at the first-stage rotor exit, 0.018 at the first-stage stator inlet, and 0.020 at all other leading- and trailing-edge locations. Blockage allowances at the hub were the same as those at the tip. The combined hub and tip blockage allowance is given in table II.

The general level of blade loading is indicated by the design diffusion factors at the tip of the first- and second-stage rotors of 0.451 and 0.410, respectively, and the first- and second-stage stators of 0.472 and 0.464, respectively. The definition used in calculating the diffusion factors is given in appendix A.

Compressor Test Facility

The two-stage fan was tested in the multistage compressor facility, which is described in detail in reference 20. A schematic diagram of the facility is shown in figure 3. Atmospheric air enters the test facility at an inlet located on the roof of the building and flows through the flow-measuring orifice, through the inlet butterfly throttle valves, and into the plenum chamber upstream of the test fan. The air then passes through the test fan into the collector and is exhausted either to the atmosphere or to an altitude exhaust system. Mass flow is controlled with a sleeve valve in the collector. For this series of tests the large inlet butterfly valve was positioned fully open to provide near atmospheric pressure at the inlet to the fan. The air was exhausted to the atmosphere.

Instrumentation

Radial surveys of the flow conditions between 1 and 30 percent of passage height from the casing were made at the fan inlet, behind each rotor, and behind the two stator-blade rows (fig. 1). Indicated values of total pressure, static pressure, total temperature, and flow angle were measured with combination probes (fig. 4). Wall static pressures were also recorded at each survey station. Each probe was aligned in the streamwise direction with a null-balancing control system. The thermocouple material was Chromel-constantan. All pressures were measured with calibrated transducers. Two combination probes were used at the compressor inlet, behind each rotor, and behind the first-stage stator; four combination probes were used behind the second-stage stator. The circumferential locations of the probes and wall static taps at each measuring station are shown in figure 5. The probes behind the stators were circumferentially traversed one stator-blade passage clockwise from the nominal values shown. The fan mass flow was determined with a calibrated thin-plate orifice located in the inlet line. An electronic speed counter, in conjunction with a magnetic pickup, was used to measure rotative speed (rpm).

The validity of using the combination probe for obtaining boundary layer measurements was established by comparison with the survey probe and boundary layer rake measurements reported in reference 24. These boundary layer rakes were used in conjunction with the combination probes when obtaining the unpublished inlet-casing boundary layer measurements used in the design of the low-aspect-ratio first stage and discussed earlier. Excellent agreement was obtained between the survey probe and the boundary

layer wakes to within 1 percent of span. This in part is attributed to the accuracy to which the probe can be positioned in the radial direction.

The errors in the data estimated from the inherent accuracy of the instrumentation and the recording systems are as follows:

Mass flow, kg/sec	±0.3
Rotative speed, rpm	±30
Flow angle, deg	±1
Temperature, K	±0.6
Total pressure (stations 1 and 2), N/cm ²	±0.07
Total pressure (station 3), N/cm ²	±0.10
Total pressure (stations 4 and 5), N/cm ²	±0.17
Indicated static pressure (stations 1, 2, and 3), N/cm ²	±0.07
Indicated static pressure (stations 4 and 5), N/cm ²	±0.17
Radial position, cm	±0.003

Test Procedure

The data for the boundary layer surveys were taken at three mass flows ranging from maximum flow to near stall at design equivalent rotative speed. At each flow condition, data were recorded at 10 radial positions at each of the five measuring stations. At the fan-inlet and rotor-exit stations (stations 1, 2, and 4), radial distributions of total pressure, static pressure, total temperature, and flow angle were recorded. At each radial position behind the stators (stations 3 and 5) the combination probes were circumferentially traversed to 10 equally spaced locations across a stator-blade gap. Values of total pressure, static pressure, total temperature, and flow angle were recorded at each circumferential position.

Data Reduction

Redundant measurements at each measuring station were arithmetically averaged. Indicated total pressures and static pressures were corrected for streamline slope, and total temperatures were corrected for recovery based on Mach number, streamline slope, and pressure environment (ref. 25). The measured temperature was then adjusted to the streamline (radial position) of the pressure measurement. All data were corrected to standard-day conditions based on values at 30 percent of the passage height at the first-stage rotor inlet. At the stator exits, radial distributions of gap-averaged (axisymmetric) parameters were obtained as follows: the circumferential distributions of total temperature were mass averaged, total pressure was energy averaged, and flow angle was arithmetically averaged. Circumferential distributions of parameters were obtained as follows: the Mach number at each radial and circumferential position behind a stator was calculated from the measured total pressure at each radial and circumferential position and an arithmetically averaged static pressure at each radial position, absolute velocity was calculated from the Mach number and measured total temperature, and absolute velocity and measured flow angle were used to calculate axial and tangential velocity components.

Selection of Static Pressure

Total-pressure, total-temperature, and flow angle measurements were taken at 10 radial positions between 1 and 30 percent of passage height from the casing. To acquire static pressures for the boundary layer surveys, the side balancing holes on the combination probes (fig. 4) were manifolded to read an indicated static pressure. Figure 6 is a comparison of the measured static pressures at station 1 from the boundary layer surveys at a mass flow of 34.23 kg/sec and calculated static pressures from full-passage-height surveys at 34.27 kg/sec (ref. 17). At 30 percent of passage height the measured static pressure was lower than the calculated static pressure.

The calculated static pressures were determined by using design end-wall blockage values. It would appear that, if the blockage value were adjusted until the calculated value at 5 percent of passage height matched the wall static value, the calculated value at 30 percent of passage height would nearly equal the measured value as well.

Since the accuracy of the static-pressure measurement was uncertain near the casing, it was assumed that a linear distribution of static pressure between the wall static and the measurement at 30 percent of passage height could be used to reduce the boundary-layer survey data. However, all measured static pressures are available from reference 18.

22-6

Boundary Layer Calculation Procedure

The procedure used in calculating the end-wall boundary layer parameters from measured data was based on a concept originally presented by van Dyke (ref. 26) and referred to as "matched asymptotic expansion." It was extended to turbomachinery flows by Mellor and Wood (ref. 6) as a means of separating the core flow from the end-wall boundary layer, flow and establishing the boundary layer edge. Ludwig and Tillman's empirical relationship (ref. 27) was used to calculate a skin friction coefficient. A similar approach is used by deRuyck and Hirsch in their axial compressor end-wall boundary layer prediction method (ref. 13). Schmidt in evaluating the performance of a sonic inlet (ref. 24) also uses this basic procedure. A detailed description of the procedure is given in appendix B. A graphical description of the inviscid velocity profile and the boundary layer profile obtained from the measured velocity profile when applying this procedure is given in figure 7.

RESULTS AND DISCUSSION

The overall and stage performance of the two-stage fan is presented in figures 8 and 9. Figures 10 to 14 show the radial distributions of various flow parameters between 1 and 20 percent of passage height at each measuring station. Figure 15 presents radial and circumferential distributions of axial velocity at the stator exits. The data in these figures are presented in tabular form in reference 18. The calculated boundary layer parameters are presented in table III. The calculated blockage factors based on measured data are compared with design values in table IV.

Overall and Stage Performance

The overall performance of the two-stage fan with the low-aspect-ratio first-stage rotor is presented in figure 8. At the design tip speed of 429 m/sec the fan achieved a peak efficiency of 0.846 at a pressure ratio of 2.471. Arrows pointing to the design speed line indicate the locations where the boundary layer data were obtained. The stage performance is given in figure 9. The first stage achieved a peak efficiency of 0.870 at a pressure coefficient of 0.257 (pressure ratio = 1.655). The second stage achieved a peak efficiency of 0.842 at a pressure coefficient of 0.260 (pressure ratio = 1.494).

A detailed examination of the blade-element data for the fan indicates that the stall line near design flow was most likely controlled by the flow in the hub region of the second stage. Unreported test results obtained on the first stage operating as a single stage indicate a stall flow of 30.8 kg/sec, which was appreciably below that for the two stages. This is further evidence that the stall line was being controlled by the second stage.

Radial Distributions at Measuring Stations

The results presented in figures 10 to 14 are for design speed at three equivalent mass flows: 34.63 kg/sec (near choke), 34.23 kg/sec (near peak efficiency), and 34.01 kg/sec (near stall). The solid lines in the figures are design values and the symbols are measured values. The boundary layer edges calculated by the previously described procedure are noted in the figures.

First-stage rotor inlet (station 1). - The wall boundary layer at the fan inlet was the most clearly identifiable and is reflected in the defect in total pressure near the wall and the associated relatively steep gradient in axial velocity (fig. 10). Since the fan did not employ an inlet guide vane, the end-wall boundary layer flow at this location was collateral, and thus a classical two-dimensional boundary layer existed. The outer casing curvature at the fan inlet (fig. 1) tended to induce an axial velocity gradient over a greater portion of the blade span than that caused by the defect in total pressure.

Note that the calculated boundary-layer-edge location determined by applying the van Dyke-Mellor-Wood approach (appendix B) was at approximately 15 percent of span from the tip (fig. 10). Even through the plots show a nearly constant total pressure beyond 10 percent of span, the tabular data presented in reference 18 show that the total pressure decreased slightly from approximately the 15 percent spanwise location. This somewhat validates the procedure for separating the inviscid effects (in this case streamline curvature) from the viscous end-wall boundary layer effect in establishing a boundary-layer-edge location. This application provides some confidence for generally applying this procedure. However, it is recognized that validation of the procedure with the two-dimensional collateral boundary layer flow at the fan inlet does not represent a complete validation of the procedure with the three-dimensional skewed boundary layer flows at the other blade-row stations.

The axial velocity was higher than design over most of the outer 30 percent of the passage height (fig. 10). This velocity difference was due at least in part to the mass flow being higher than design. The measured velocity decreased rapidly from 5 percent of span to the outer wall, and this was consistent with the decrease in total pressure. The tempered total-pressure gradient used in the design at the rotor inlet resulted in a radial mismatch in relative flow angle and thus in incidence angle from design, as would

be expected. The comparison of design and measured total-pressure distributions through the end-wall region illustrates a design problem. The measured total-pressure profile reflects the real flow loss gradient, but the design total-pressure profile reflects the approximate loss gradients that can be accommodated in typical axisymmetric design calculations. The differences resulted in the need for an end-wall flow blockage correction and an unavoidable mismatch in relative flow angle and incidence angle from the design intent. This same reasoning, of course, applies at all blade-row inlet and outlet stations. A slight increase in total temperature was detected that is difficult to explain but often observed.

First- and second-stage rotor exits (stations 2 and 4). - Similar trends in the radial distribution of flow parameters existed at the first- and second-stage rotor exits (figs. 11 and 13). From approximately 10 percent of span to the outer wall the parameters deviated appreciably from free-stream values, reflecting the impact of the end-wall boundary layer on these parameters. The calculated boundary layer edge was in close proximity to the rapid falloff in velocity. For both rotor rows the penetration of the high-loss region (composed of end-wall boundary layer and associated secondary flows) into the free stream was approximately one-half that of the staggered spacing, a penetration parameter suggested by Smith (ref. 4).

As shown by the radial distributions of flow angles in figures 11 and 13, the boundary layer flow behind the rotors was a highly skewed, three-dimensional flow, in contrast to the two-dimensional end-wall boundary layer that existed at the first-stage rotor inlet. The data show axial velocities in the high-shear end-wall region that are appreciably lower than free-stream values and are consistent with the decay in total pressure near the wall. The lower axial velocities resulted in higher end-wall energy additions, as reflected in the tangential velocities and the temperature. This higher energy addition existed even though the relative flow angles reflected higher deviation angles and lower relative flow turning than free-stream values. The lower end-wall total pressure coupled with the high temperature reflected a low tip-region efficiency for the first stage. It was not as obvious for the second stage because of the radial gradients in flow parameters at both the rotor inlet and exit. However, close examination revealed the same to be true for the second stage. The much higher than design absolute flow angles in the end-wall region at the rotor exits reflected a higher than design incidence coming into the stators.

First- and second-stage stator exits (stations 3 and 5). - The trends in flow parameters behind the stators (figs. 12 and 14) were similar to those observed behind the rotors (figs. 11 and 13). However, the magnitude of the gradients was greatly reduced. The tempering of the end-wall gradients as the flow passed through the stator was particularly evident when comparing the axial velocity profiles between stations. The gradient in axial velocity near the wall at the stator-exit measuring stations (figs. 12 and 14) was much less than that at the rotor-exit measuring stations (figs. 11 and 13). From figures 12 and 13 it can be seen that the total-temperature profile leaving the first-stage rotor was redistributed as it passed through the following stator. Measured total temperatures near the wall at the stator exit were lower than the corresponding temperatures at the rotor exit. Conversely, total temperatures in the free-stream region were higher at the first-stage stator exit than at the first-stage rotor exit. This redistribution of total temperature is considered to be a result of mixing. It is reasoned that the mixing would increase with larger axial spacing between blades and thus could be greater for this fan than for fans with closely coupled blade rows. Note that the calculated boundary-layer-edge location was far inboard of the more noted falloff in axial velocity. This could also be a result of flow mixing. The plots of absolute flow angle show a 6° overturning of the flow near the casing (past the 0° design outlet flow angle) at the first-stage stator exit and a 4° overturning of the flow at the second-stage stator exit. This reflects the strength in the crossflow component from the pressure surface to the suction surface within the stator passage.

Circumferential Distributions at Stator Exit Stations

The radial and circumferential distributions of axial velocity behind the first- and second-stage stators (stations 3 and 5) are plotted in figure 16 for a mass flow of 34.23 kg/sec. For clarity, only 5 of the 10 radial positions at each station are plotted. The wakes behind both stators were less pronounced at 30 percent of the passage height than at 3 or 4 percent of the passage height. This reflects an increase in flow blockage caused by the nonaxisymmetric flow field near the walls. The wake also appeared to shift circumferentially toward the pressure side of the blade near the tip of both stators. This reflects the crossflow component from the pressure surface to the suction surface, which results in the overturning noted earlier. The axial velocity at the edge of the wake on the suction side of the blade was significantly lower than the corresponding velocity at the tip on the pressure side. This velocity imbalance existed at 1 and 2 percent of passage height and was nearly gone at 3 or 4 percent of passage height. The data indicate that the gap-average profile used in the boundary layer calculations did contain secondary flow effects and that the classical boundary layer parameters calculated from the measured data reflect the presence of this secondary flow field.

Boundary Layer Calculations

The boundary layer parameters calculated from the measured data are presented in table III. Only small differences are noted between the different flow points. This might be expected because of the relative closeness of the points, coupled with the fact that the fan did not appear to be tip critical, as discussed earlier. It is reasoned that only when the tip is critical would an increase in displacement thickness and flow blockage be expected for the tip when near stall. It is interesting that an incompressible form factor of 1.5 or less for all axial stations and flow points was calculated since it is generally accepted that an incompressible form factor in the range of 1.8 to 2.2 signals separation of a two-dimensional collateral boundary layer. This would appear to be additional evidence that the tip flow across the fan did not initiate stall.

The easiest parameter to examine in order to get a physical insight and appreciation for the boundary layer calculation is the blockage factor. With the blockage being one minus the blockage factor the conversion was made to compare measured blockages with design values in table IV. Before discussing the comparisons one must consider what constitutes the blockage calculated from the measured data and what the design blockage allowance represents. The radial distribution of axial velocity used to calculate an end-wall boundary layer is influenced by a number of factors. Two of these factors (fig. 16) are inviscid: streamline curvature in the meridional plane and varying energy levels of the streamlines along the blade span. The latter factor generally results from a radially varying work input from the rotor rows. Both of these factors can either increase or decrease the level of axial velocity in the end-wall region. Factors that are viscous are the radial distribution of flow losses and a blockage type of effect due to a nonaxisymmetric flow field. The radial distribution of losses includes the blade profile loss, shock loss, end-wall boundary layer loss, and secondary flow losses. The latter two loss sources are stronger in the end-wall flow region. The blockage effect due to nonaxisymmetric flows must be applied whenever circumferentially mass-averaged parameters, in particular total pressure, are used to compute the gap-averaged flow velocities. This accounts for the mass flow differences when flow, which is an area-averaged quantity, is computed from mass-averaged parameters. Hence the need to consider such a blockage when applying design procedures, through-flow analyses, some data analyses, etc., where pressures, temperatures, and angles used to compute the velocity field are, or are assumed to be, mass-averaged quantities. The nonaxisymmetric flow field and associated blockages are discussed in detail by Dring in references 28 and 29.

The difference between measured and design blockage allowances is shown in figure 17. Typically the design procedures partially account for the higher loss levels in the end-wall regions but cannot accommodate the very severe gradients through the end-wall boundary layer flows. Hence the need for an end-wall blockage exists. In most cases the spanwise blockages associated with nonaxisymmetric flows are unknown and are added to the end-wall blockage. As figure 17 shows, the measured blockage is the sum of the equivalent blockage associated with the design end-wall loss gradient K_1 and the design end-wall blockage allowance K_2 . The design blockage allowance includes the design end-wall blockage allowance K_2 and the blockage associated with the non-axisymmetric flow field K_3 .

The foregoing discussion delineates some of the flow physics in the compressor end-wall flow regions that necessitates the use of blockage factors in design and analysis procedures and points to the difficulty of extracting the needed parameters from measured data. Hence a comparison of the design and measured blockages is a subjective one at present. The comparisons for this fan are presented in table IV.

In general, the level of measured blockage agreed reasonably well with the design values. For the first-stage rotor the measured blockage was somewhat higher than design, and for the exit of the second stator it was somewhat lower than design. The measured blockages did reflect an increase through the rotors and a decrease through the stators. Also the measured blockage for the second stage was essentially the same as that for the first stage. This could be due in part to the flow mixing noted earlier.

It was recognized that meaningful blockage factors can be obtained from compressor end-wall experimental measurements only if the selection of the boundary layer thickness (edge) effectively accounts for all of the viscous flow effects and ignores the inviscid flow effects. The van Dyke procedure described in appendix B was selected for this study since it had these capabilities. Some judgment on the worthiness of the van Dyke-Mellor-Wood procedure can be made by applying it to the fan inlet flow. At the fan inlet the total-pressure distribution indicates the spanwise extent of the viscous effects, and the axial velocity distribution indicates that local streamline curvature effects are also present.

As noted previously the calculated boundary-layer-edge location determined by applying the van Dyke-Mellor-Wood approach (appendix B) is at approximately 15 percent of span from the tip (fig. 10). Even though the plots show a nearly constant total pressure beyond 10 percent of span, the tabular data presented in reference 18 show the total pressure to decrease, starting at approximately 15 percent of span. This somewhat validates the procedure for separating the inviscid effects (in this case streamline curvature) from the viscous end-wall boundary layer effect in establishing a boundary-layer-edge location. This application provides some confidence for generally applying this procedure. However, it is recognized that validation of the procedure with the two-dimensional, collateral boundary layer flow at the fan inlet does not represent a

complete validation of the procedure with the three-dimensional, skewed boundary layer flows at the other blade-row stations.

To provide an indication of the sensitivity of the boundary layer parameters to the selected boundary layer thickness (edge), the boundary layer parameter J were calculated from the measured profiles by arbitrarily selecting the boundary layer edge at various spanwise locations along the measured velocity profile. This standard boundary layer procedure is illustrated in graphical form in figure 18 and the results of the calculations are shown in figure 19. The data presented in figure 19 are for the near-peak-efficiency flow point. Plots of axial and tangential momentum thickness and axial displacement thickness are presented as a function of spanwise location of the assumed boundary layer edge for each of the five axial locations. As can be noted from the figure, the magnitude of the calculated boundary layer parameters is a relatively strong function of the assumed boundary-layer-edge location. At stations behind the rotors the calculated boundary layer parameters tend to level off in the region where one might assume the boundary layer edge to be (figs. 11 and 13) and the edge value determined by the procedure presented in appendix B. However, at the first-stage rotor inlet and at the exits of each stator the boundary layer parameters continue to increase as the assumed boundary-layer-edge location is moved to larger percentages of the span. This is particularly true at station 1 and can be attributed to stronger streamline curvature effects at this station. In any case the data presented in figure 19 reflect the need for a sound procedure for establishing the boundary-layer-edge location in a flow field that includes both inviscid and viscous effects in terms of the governing factors controlling the velocity profiles. Although the van Dyke-Mellor-Wood procedure for selecting the end-wall boundary layer edge downstream of rotors and stators cannot be firmly established as valid from the data, it represents the consistent procedure needed to carry out an extended correlation of end-wall boundary layer parameters.

CONCLUDING REMARKS

The detailed boundary layer measurements obtained in the high-tip-speed, high-pressure-ratio two-stage fan extend the experimental data base for end-wall boundary layer modeling and code verification. Various factors that contribute to the flow blockage through a compressor were discussed. The blockage based on measured data was related to the blockage used in the design and analysis procedures.

Because specific design and performance features of this fan probably influenced the data, some care should be exercised in applying these results in general. These features included

1. Wide axial spacing between blade rows (to alleviate noise generation). This provided an unusually long flow path for enhanced flow mixing, which appeared to have a significant effect on end-wall gradients and blockage values.

2. High reaction stages (large static pressure rise across the rotors and low static pressure rise across the stators). This may have a significant influence on the trend of an increase in blockage across the rotors and a decrease across the stators.

3. Fan stall initiated in hub region of second stage. This probably was responsible for the nearly constant tip blockage over the flow range covered.

A need therefore exists to provide data to permit generalizing and quantifying the influence of the various design and performance features on the end-wall flows.

Two recent methods to calculate the factors directly or indirectly affecting flow blockages have recently been introduced. One is the method proposed by Adkins and Smith in reference 16 for calculating the spanwise mixing of the flow as it passes through a multistage compressor. This method can be applied directly to a design or analysis procedure. The second is an approach to calculating the spanwise distribution of blockage due to nonaxisymmetric flows proposed by Dring in references 28 and 29. This approach requires detailed gapwise measurements at the rotor-exit stations and at the stator-exit stations to obtain the pertinent data. Both of these methods must be supported by relevant experimental data.

Finally, the data presented reflect the need for improved design approaches (methods) to more accurately account for the significant departures in the flow parameters in the end-wall boundary layer region in relation to free-stream values. The results of a program conducted on a large low-speed compressor to address this need are summarized by Wisler in reference 30. Various designs incorporating end-wall bends into the stator blade rows to accommodate the highly skewed end-wall profiles were studied. The effects of these design concepts on efficiency and stall margins as well as on the local blade-surface velocity distributions were presented.

SUMMARY OF RESULTS

This report presents detailed measurements of the casing boundary layer in a 429-m/sec-tip-speed, two-stage fan. The fan achieved a peak adiabatic efficiency of 0.851 at a pressure ratio of 2.433 at design speed. The principal results from the measured data were as follows:

ORIGINAL PAGE IS OF POOR QUALITY

22-10

1. The measured radial distributions of flow parameters obtained in the casing boundary layer showed sharp departures from the free-stream values at all survey stations near the casing wall.

2. In this high-shear end-wall flow region at the rotor exit the following combination of flow conditions existed: low axial velocity, high energy addition, low pressure, low efficiency, high relative flow angles, and large deviation angles. The low absolute velocity measured at the rotor exits near the casing reflected a high incidence on the stator.

3. In the end-wall flow regions downstream of the stators, decreased gradients and increased spanwise penetration of the end-wall boundary layer (as compared with the rotor exit) indicated that some mixing occurred in the flow across stator rows. Significant overturning of flow close to the outer wall was evident.

4. Over the complete flow range at 100 percent of design speed the calculated casing boundary layer parameters showed only small variations with operating conditions. No indication of boundary layer separation was apparent during near-stall operation.

5. For this fan the tip annulus boundary layer and associated flow blockage increased across the rotors and decreased across the stators. The calculated blockages for the second stage based on measured data were essentially the same as those for the first stage.

APPENDIX A

EQUATIONS

Diffusion factor

$$D = 1 - \frac{V_{TE}}{V_{LE}} + \frac{(rV_\theta)_{TE} - (rV_\theta)_{LE}}{(r_{TE} + r_{LE})\sigma(V_{LE})} \quad (A1)$$

Percent of passage height

$$\frac{(r_t - r)}{(r_t - r_h)} 100 \quad (A2)$$

Adiabatic (temperature rise) efficiency

$$\eta_{ad} = \frac{\frac{P_{TE}}{P_{LE}}^{(\gamma-1)/\gamma} - 1}{\frac{T_{TE}}{T_{LE}} - 1} \quad (A3)$$

Equivalent mass flow

$$W\sqrt{\theta}/\delta \quad (A4)$$

Equivalent rotative speed

$$N/\sqrt{\theta} \quad (A5)$$

Head-rise coefficient

$$P = \frac{C_P T_{LE}}{U_{tip}^2} \left[\left(\frac{P_{TE}}{P_{LE}} \right)^{(\gamma-1)\gamma} - 1 \right] \quad (A6)$$

Flow coefficient

$$\phi = \frac{V_z}{(U_{tip})_{LE}} \quad (A7)$$

Polytropic efficiency

$$\eta_p = \frac{\ln \left(\frac{P_{TE}}{P_{LE}} \right)^{(\gamma-1)/\gamma}}{\ln \left(\frac{T_{TE}}{T_{LE}} \right)} \quad (A8)$$

Temperature-rise coefficient

$$\psi_T = \frac{C_p (T_{TE} - T_{LE})}{U_{tip}^2} \quad (A9)$$

Relative flow angle

$$\beta' = \arctan \left(\frac{V'_\theta}{V'_z} \right) \quad (A10)$$

Blockage factor

$$K_b = \frac{(r_t - \delta^*)^2 - (r_h + \delta_h^*)^2}{r_t^2 - r_h^2} + K_3 \quad (A11)$$

Blockage from nonaxisymmetric flows

$$K_3 = \frac{(\bar{V}_z)_{\text{based on area average}}}{(\bar{V}_z)_{\text{based on mass-averaged properties}}} \quad (A12)$$

APPENDIX B

BOUNDARY LAYER REDUCTION PROCEDURE

Devising a method for separating the inviscid rotational core flow from the end-wall boundary layer flow is complicated by the fact that the free stream (edge of the boundary layer) velocity is unknown. By using an approximate engineering approach, the following turbulent boundary layer data reduction program was developed.

From van Dyke's original concept (ref. 26) and as suggested for internal flows by Mellor and Wood (ref. 6), the measured velocity across an annular passage with total-pressure variation is given by

$$U_{\text{meas}} = U_b + U_{\text{inv}} - U_e \quad (B1)$$

where U_{meas} is the measured velocity profile, U_b is the boundary layer velocity profile, U_{inv} is the curve-fitted inviscid velocity profile, and U_e is the free-stream (edge of the boundary layer) velocity. A graphical description of the inviscid, measured, and calculated boundary layer velocity profiles is given in figure 7.

Assuming an initial value for U_e , the outer values of the inviscid velocity profile U_{inv} were curve fitted to the wall value U_e . With the measured velocity profile U_{meas} and an initially assumed U_e , the boundary layer velocity profile U_b was calculated from equation (B1). The boundary layer integrations were then performed to obtain the following momentum and displacement thicknesses:

$$\theta = \int_0^\delta \left(1 - \frac{U_b}{U_e} \right) \frac{\rho}{\rho_e} \frac{U_b}{U_e} dy \quad (B2)$$

$$\delta^* = \int_0^\delta \left(1 - \frac{\rho}{\rho_e} \frac{U_b}{U_e} \right) dy \quad (B3)$$

ORIGINAL PAGE IS
OF POOR QUALITY

22-12

where θ is the momentum thickness, δ^* is the displacement thickness, y is the boundary layer distance from the wall, δ is the edge of the boundary layer distance, and ρ is the density.

The compressible form factor H_C and the incompressible form factor H_i are

$$H_C = \frac{\delta^*}{\theta} \quad (B4)$$

$$H_i = \left(H_C - Pr^{1/3} \gamma \frac{M_\infty^2}{2} \right) / \left(1 + \frac{\gamma}{2} M_\infty^2 \right) \quad (B5)$$

where Pr is the Prandtl number set at 0.71, γ is the ratio of specific heats, and M_∞ is the Mach number at the edge of the boundary layer.

With U_∞ , H_i , and θ already calculated, the skin friction coefficient C_f was calculated by using Ludwig and Tillman's relationship from reference 27

$$\frac{C_f}{2} = 0.123 \left(e^{-1.561 H_i} \right) \left(\frac{\mu_{ref}}{\rho_\infty U_\infty \theta} \right) \left(\frac{t_\infty}{t_{ref}} \right) \quad (B6)$$

where μ_{ref} is the dynamic viscosity based on reference temperature and the reference temperature t_{ref} is

$$t_{ref} = t_\infty \left(1.0 + 0.72 Pr^{1/3} \gamma \frac{M_\infty^2}{2} \right) \quad (B7)$$

where t_∞ is the static temperature at the edge of the boundary layer.

From the already determined boundary layer parameters and Cole's law of the wake the shear velocity can be calculated. Cole's law of the wake is

$$\frac{U}{U_\tau} = \frac{1}{K_1} \ln \left(\frac{\rho U_\tau y}{\mu} \right) + C_1 + \frac{2H(x)}{K_1} W \left(\frac{y}{\delta} \right) \quad (B8)$$

where $K_1 = 0.40$, $C_1 = 5.1$, U_τ is the local air velocity at each point in the boundary layer, $H(x)$ is a parameter describing the velocity defect law, and $W(y/\delta)$ is a wavelike function describing the outer wake region of the boundary layer.

At the boundary layer edge $U = U_\infty$, and equation (B8) becomes

$$\frac{U_\infty}{U_\tau} = \frac{1}{(C_f/2)^{1/2}} = \frac{1}{K_1} \ln \left(\frac{\rho_\infty U_\tau \delta}{\mu_\infty} \right) + C_1 + \frac{2H(x)}{K_1} \quad (B9)$$

solving for $2H(x)/K_1$ in equation (B9) gives

$$\frac{2H(x)}{K_1} = \frac{1}{(C_f/2)^{1/2}} - C_1 - \frac{1}{K_1} \ln \left(\frac{\rho_\infty U_\tau \delta}{\mu_\infty} \right) \quad (B10)$$

Solving for U_τ in equation (B8) gives

$$U_\tau = \frac{U_n}{\frac{1}{K_1} \ln \left(\frac{\rho_n U_\tau y_n}{\mu_n} \right) + C_1 + \frac{2H(x)}{K_1} W \left(\frac{y}{\delta} \right)} \quad (B11)$$

where

$$W \left(\frac{y}{\delta} \right) = 2 \sin^2 \left(\frac{\pi}{2} \frac{y}{\delta} \right) \quad (B12)$$

and n is the measured boundary layer point for evaluating U , y , ρ , and μ . Initially, the shear velocity U_τ was estimated from the shear stress equation as

$$U_\tau = U_\infty \left(\frac{C_f}{2} \right)^{1/2} \quad (B13)$$

ORIGINAL PAGE IS
OF POOR QUALITY

22-13

Then equation (B11) was iterated for the correct U_t . The iterated U_t was obtained for

- $n = 1$ (first measured point);
 $n = 2$ (second measured point)

The U_t 's calculated by using the first and second points were then averaged to obtain the new U_t . From this U_t and equation (B13) a new U_e can be obtained

$$U_e = \frac{U_t}{(C_F/2)^{1/2}} \quad (B14)$$

With this new U_e the complete iteration loop was repeated until the new U_e had negligible change from the old U_e .

REFERENCES

1. Bailly, J. W.; and Howard, J. H. G.: Velocity Profile Development in Axial Flow Compressors. *J. Mech. Eng. Sci.*, vol. 4, no. 2, Apr. 1962, pp. 166-176.
2. Cooke, J. A.; and Hall, M. G.: Boundary Layers in Three Dimensions. *Progress in Aeronautical Sciences*, vol. 2, A. Ferri, D. Kuchemann, and L. H. G. Sterne, eds., Pergamon Press, 1962, pp. 221-282.
3. Stratford, B. S.: The Use of Boundary Layer Techniques to Calculate the Blockage from the Annulus Boundary Layers in a Compressor. ASME Paper 67-WA/GT-7, 1967.
4. Smith, L. H.: Casing Boundary Layers in Multistage Axial Flow Compressors. *Flow Research on Blading*, L. S. Dzung, ed., Elsevier, 1970, pp. 275-304.
5. Horlock, J. H.: Boundary Layer Problems in Axial Turbomachines. *Flow Research on Blading*, L. S. Dzung, ed., Elsevier, 1970, pp. 322-371.
6. Mellor, G. L.; and Wood, G. M.: An Axial Compressor End-Wall Boundary Layer Theory. *J. Basic Eng.*, vol. 93, 1971, pp. 300-316.
7. Marsh, H.; and Horlock, J. H.: Wall Boundary Layers in Turbomachines. *J. Mech. Eng. Sci.*, vol. 14, no. 6, Dec. 1972, pp. 411-423.
8. Daneshyar, M.: Annulus Wall Boundary Layers in Turbomachines. Ph.D. Thesis, Cambridge University, 1973.
9. Horlock, J. H.; and Perkins, H. J.: Annulus Wall Boundary Layers in Turbomachines. AGARD AG-185, 1974.
10. Hirsch, C.: End-Wall Boundary Layers in Axial Compressors. ASME Paper 74-GT-72, Mar. 1974.
11. deRuyck, J.; Hirsch, C.; and Kool, P.: An Axial Compressor End-Wall Boundary Layer Calculation Method. *J. Eng. Power*, vol. 101, no. 2, Apr. 1979, pp. 233-249.
12. deRuyck, J.; Hirsch, C.; and Kool, P.: Investigation on Axial Compressor End-Wall Boundary Layer Calculations. Presented at the International Joint Gas Turbine Congress (Haifa, Israel), July 1979.
13. deRuyck, J.; and Hirsch, C.: Investigations on an Axial Compressor End-Wall Boundary Layer Prediction Method. *J. Eng. Power*, vol. 103, no. 1, Jan. 1981, pp. 20-33.
14. Hirsch, C.; and Denton, J. D., eds.: Through Flow Calculations in Axial Turbomachines. AGARD Advisory Report No. 175, Oct. 1981.
15. Koch, C. C.; and Smith, L. H., Jr.: Loss Sources and Magnitudes in Axial-Flow Compressors. ASME Paper 75-WA/GT-6, Nov. 1975.
16. Adkins, G. G., Jr.; and Smith, L. H., Jr.: Spanwise Mixing in Axial-Flow Turbomachines. ASME Paper 81-GT-57, Mar. 1981.
17. Urasek, D. C.; Gorrell, W. T.; and Cunnann, W. S.: Performance of a Two-Stage Fan Having Low-Aspect-Ratio First-Stage Rotor Blading. AVRADCOM TR-78-49, NASA TP-1493, Aug. 1979.
18. Gorrell, W. T.: Detailed Flow Measurements in Casing Boundary Layer of 427-Meter-Per-Second-Tip-Speed Two-Stage Fan with Casing Treatment. AVRADCOM TR-81-C-28, NASA TP-2052, Jan. 1983.
19. deRuyck, J.; and Hirsch, C.: End-Wall Boundary Layers in Multistage Axial Compressors. AGARD Paper 61-A-19, June 1983.
20. Cunnann, W. S.; Stevans, W.; and Urasek, D. C.: Design and Performance of a 427-Meter-per-Second-Tip-Speed Two-Stage Fan Having a 2.40 Pressure Ratio. NASA TP-1314, Oct. 1978.

ORIGINAL PAGE IS
OF POOR QUALITY

22-14

21. Urasek, D. C.; Cunnah, W. S.; and Stevens, W.: Performance of Two-Stage Fan with Larger Damper on First-Stage Rotor. NASA TP-1399, May 1979.
22. Gorrell, W. T.; and Urasek, D. C.: Performance of Two-Stage Fan with a First-Stage Rotor Redesign to Account for the Presence of a Part-Span Damper. AVRADCOM TR-79-10, NASA TP-1483, Sept. 1979.
23. Ball, C. L.; Janetzke, D. C.; and Reid, L.: Performance of 1380-Foot-Per-Second-Tip-Speed Axial-Flow Compressor Rotor with Blade Tip Solidity of 1.1. NASA TM X-2449, Mar. 1972.
24. Schmidt, J. F.; and Ruggeri, R. S.: Performance and Boundary-Layer Evaluation of a Sonic Inlet. NASA TN D-8340, Nov. 1976.
25. Glawe, G. E.; Krause, L. N.; and Dudzinski, T. J.: A Small Combination Sensing Probe for Measurement of Temperature, Pressure, and Flow Direction. NASA TN D-4816, Oct. 1968.
26. van Dyke, M. D.: Perturbation Methods in Fluid Mechanics. Academic Press, 1964, pp. 81-97.
27. Sasman, P. K.; and Cresci, R. J.: Compressible Turbulence Boundary Layer with Pressure Gradient and Heat Transfer. AIAA J. vol. 4, no. 1, Jan. 1966, pp. 19-25.
28. Dring, R. P.; Wagner, J. H.; and Joslyn, H. D.: Axial Compressor Middle Stage Secondary Flow Study. NASA CR in preparation, 1983.
29. Dring, R. P.; Joslyn, H. D.; and Wagner, J. H.: Compressor Rotor Aerodynamics. AGARD Paper 61-A-24, June 1983.
30. Wisler, D. C.: Core Compressor Exit Stage Study, VI - Final Report. (GE-R81AEG-288, General Electric Co., NASA Contract NAS3-20070.) NASA CR-165553, Dec. 1981.

TABLE I. - OVERALL DESIGN PARAMETERS

(a) Two-stage fan

Fan total-pressure ratio	2.399
Fan total-temperature ratio	1.334
Fan adiabatic efficiency	0.849
Fan polytropic efficiency	0.866
Weight flow, kg/sec	33.248
Weight flow per unit frontal area, kg/sec m ²	162.381
Weight flow per unit annulus area, kg/sec m ²	189.016
Rotative speed, rpm	16042.800
Tip speed, m/sec	428.896

(b) First stage

Rotor total-pressure ratio	1.629
Stage total-pressure ratio	1.590
Rotor total-temperature ratio	1.167
Stage total-temperature ratio	1.167
Rotor adiabatic efficiency	0.895
Stage adiabatic efficiency	0.848
Rotor polytropic efficiency	0.903
Stage polytropic efficiency	0.857
Rotor head-rise coefficient	0.236
Stage head-rise coefficient	0.223
Flow coefficient	0.429

(c) Second stage

Rotor total-pressure ratio	1.537
Stage total-pressure ratio	1.509
Rotor total-temperature ratio	1.143
Stage total-temperature ratio	1.143
Rotor adiabatic efficiency	0.911
Stage adiabatic efficiency	0.870
Rotor polytropic efficiency	0.917
Stage polytropic efficiency	0.877
Rotor head-rise coefficient	0.267
Stage head-rise coefficient	0.256
Flow coefficient	0.464

TABLE II. - FAN DESIGN
BLOCKAGE ALLOWANCES

	Inlet	Outlet
	Blockage, percent	
Rotor 1	2.0	2.6
Stator 1	3.6	4.0
Rotor 2	4.0	4.0
Stator 2	4.0	4.0

TABLE III. - MEASURED BOUNDARY LAYER PARAMETERS

Sta- tion	Edge velocity, U_e , m/sec	Mach number, M_0	Boundary layer edge, δ , cm	Axial momentum thickness, δ_x , cm	Axial displace- ment thickness, δ^* , cm	Tangential momentum thickness, δ_{τ} , cm	Blockage factor, K_b	Axial incom- pressible form factor, H_1	Skin friction coefficient, $C_f/2$	Linear velocity, U_e , m/sec
Mass flow = 14.63 kg/sec (near choke)										
1	194.7	0.591	2.326	0.1375	0.2009	-----	0.902	1.309	0.00246	9.66
2	204.0	.570	1.545	.1038	.3103	-0.0567	.967	1.530	.00147	7.01%
3	182.7	.503	1.213	.1220	.1722	.0185	.900	1.290	.00259	9.296
4	178.0	.460	0.830	.1305	.2042	.02423	.972	1.460	.00183	7.650
5	176.1	.452	0.846	.0716	.0792	.02536	.906	1.300	.00299	9.630
Mass flow = 34.23 kg/sec (near peak efficiency)										
1	193.6	0.506	2.362	0.1481	0.2164	-----	0.980	1.31	0.00240	9.40
2	195.1	.540	1.219	.1505	.2524	-0.0460	.973	1.46	.00175	8.15
3	186.4	.509	1.515	.1049	.1404	.0093	.903	1.31	.00263	9.56
4	167.7	.424	0.671	.1067	.1631	.00393	.970	1.44	.00206	7.61
5	175.0	.444	1.073	.0607	.0856	.0257	.900	1.32	.00299	9.62
Mass flow = 34.01 kg/sec (near stall)										
1	191.10	0.579	2.131	0.1399	0.2036	-----	0.982	1.31	0.00247	9.49
2	196.6	.547	2.042	.1750	.2806	-0.0472	.969	1.50	.00150	7.82
3	189.5	.510	1.853	.1085	.1539	-.00012	.902	1.30	.00258	9.63
4	177.0	.451	0.830	.1190	.1850	-.00005	.975	1.45	.00191	7.76
5	173.1	.437	0.844	.0604	.0826	.0295	.900	1.29	.00321	9.81

TABLE IV. - COMPARISON BETWEEN
DESIGN AND MEASURED BLOCKAGES

[Tip values at measuring station,
near peak efficiency.]

$$[K_{\text{mean}} = K_1 + K_2; K_{\text{des}} = K_2 + K_3]$$

	Design Measured	
	Blockage, percent	
Rotor 1 inlet	1.0	2.0
Rotor 1 outlet	1.5	2.7
Stator 1 outlet	2.0	1.7
Rotor 2 outlet	.0	2.2
Stator 2 outlet	0	1.2

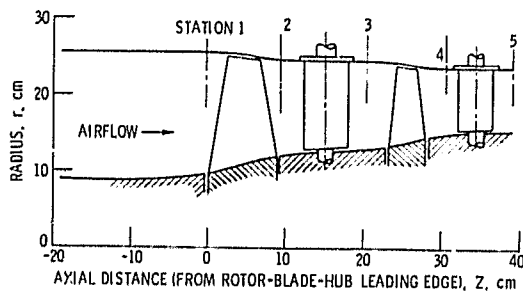


Figure 1. - Flow path of two-stage low-aspect-ratio fan.

Flow path coordinates

Axial distance, Z , cm	Radius, r , cm	
	Outer	Inner
-13.093	25.654	8.994
-8.016	25.654	8.903
-2.936	25.654	9.093
^a -2.203	25.651	9.543
2.144	25.570	10.160
4.684	25.128	10.973
7.224	24.681	11.565
^a 9.764	24.460	11.902
12.304	24.384	12.139
14.844		12.438
17.384		12.822
19.924		13.022
^a 20.803		13.038
22.464	24.328	13.152
25.004	23.993	13.627
27.544	23.655	14.371
^a 30.084	23.622	14.699
32.177		14.849
36.754		15.237
^a 38.850		15.240
42.784		15.240

^aInstrument survey plane.

ORIGINAL PAGE IS
OF POOR QUALITY

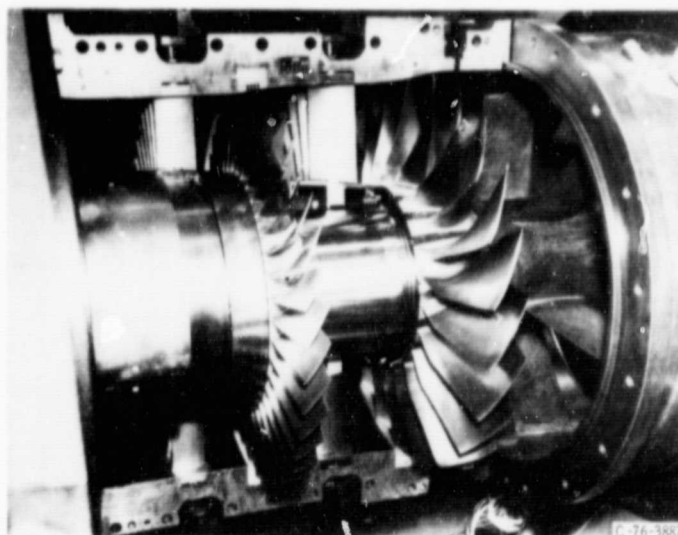


Figure 2. - Two-stage fan with low-aspect-ratio, first-stage rotor.

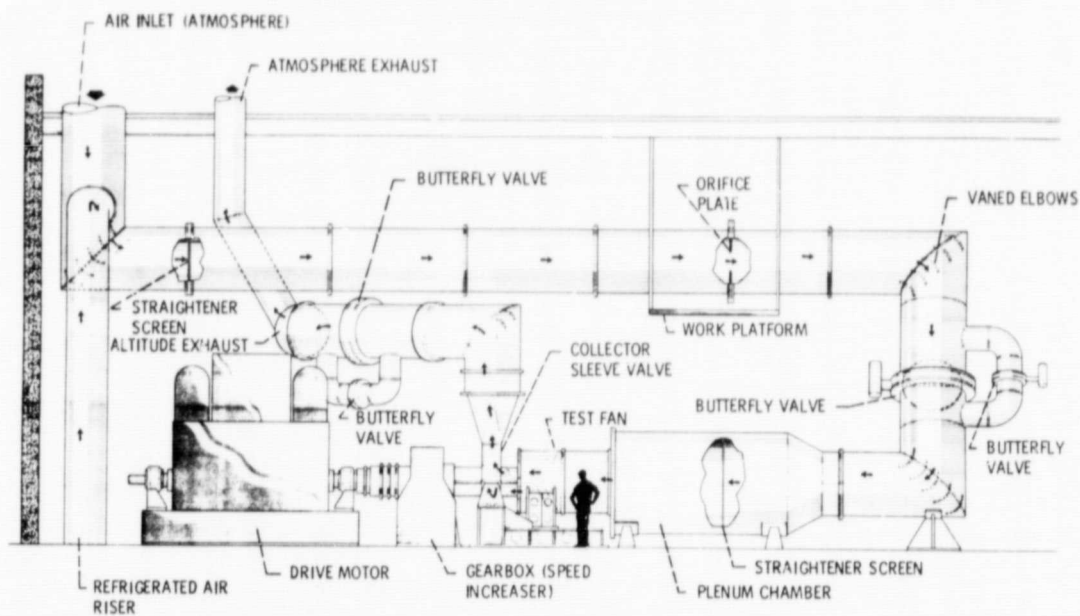


Figure 3. - Multistage compressor test facility.

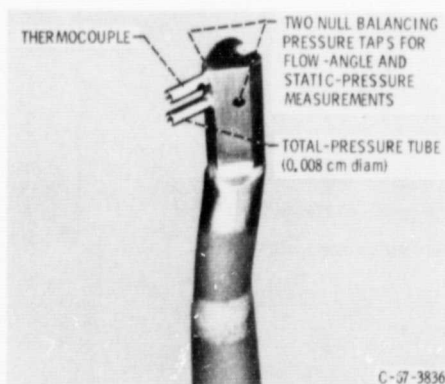
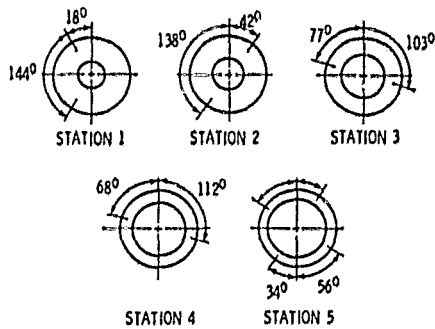
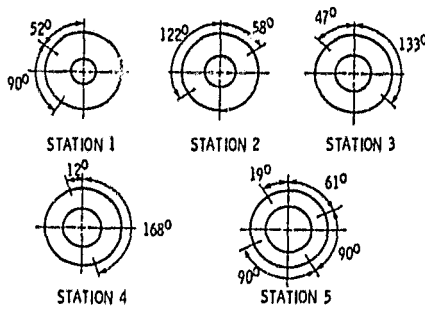


Figure 4. - Combination total-pressure, static-pressure, total-temperature, and flow-angle probe (double barrel).



(a) Combination probes.



(b) Static-pressure taps.

Figure 5. - Circumferential locations of instrumentation at measuring stations (looking downstream).

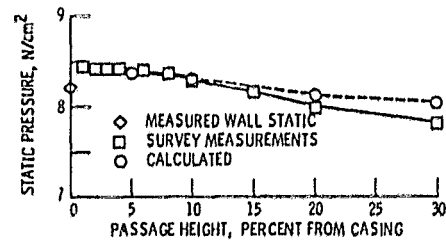


Figure 6. - Comparison of measured and calculated static pressure at station 1.

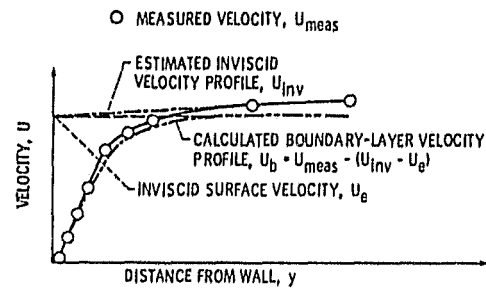


Figure 7. - Graphical description of inviscid, measured, and calculated velocity profiles.

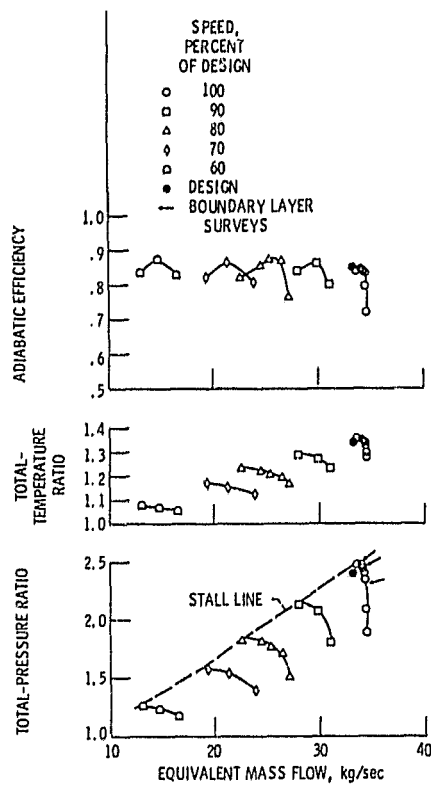


Figure 8. - Overall performance of two-stage, low-aspect-ratio fan.

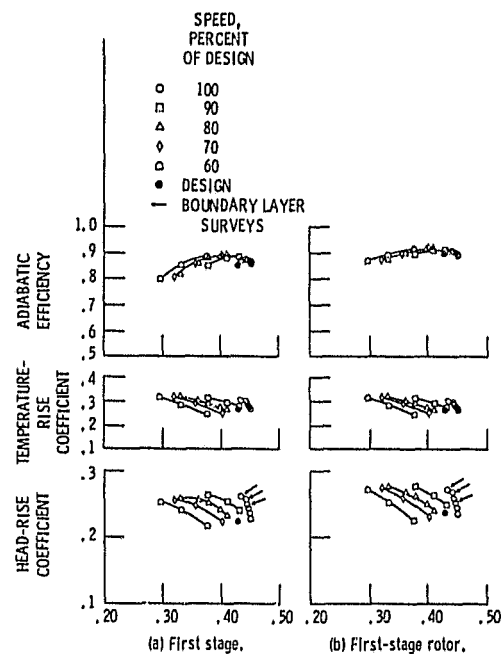
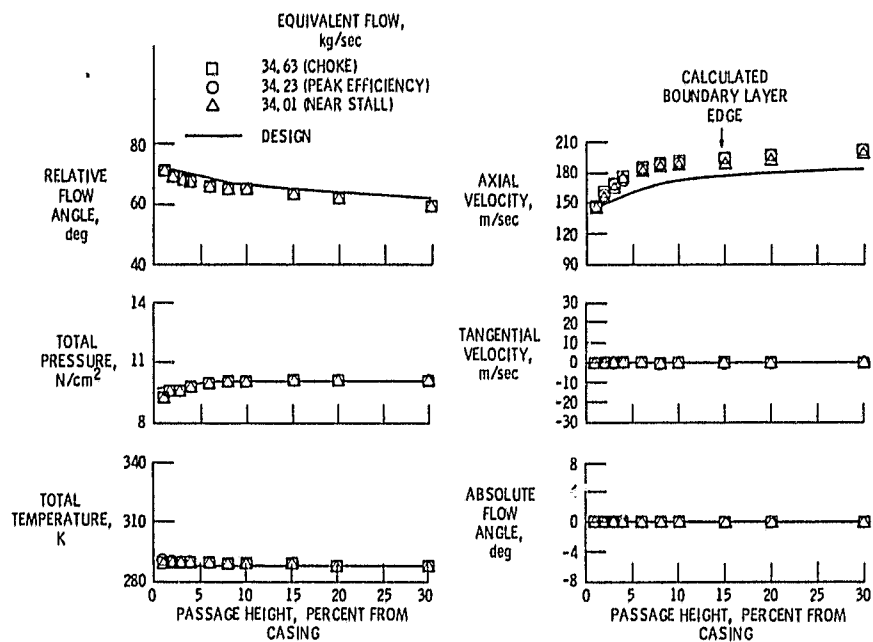
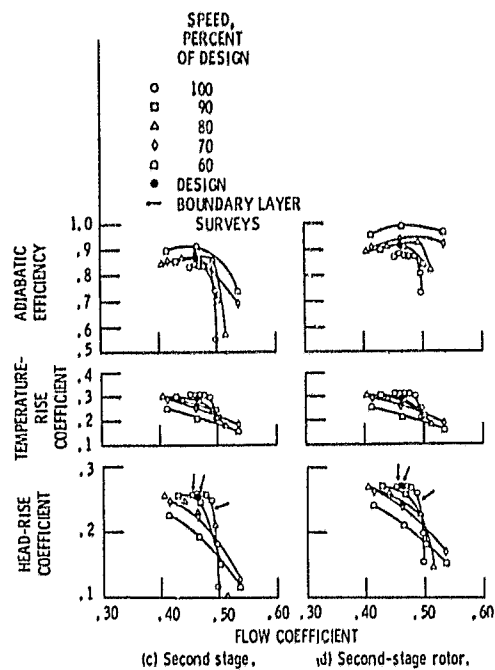


Figure 9. - Dimensionless overall performance.

ORIGINAL PAGE 13
OF POOR QUALITY



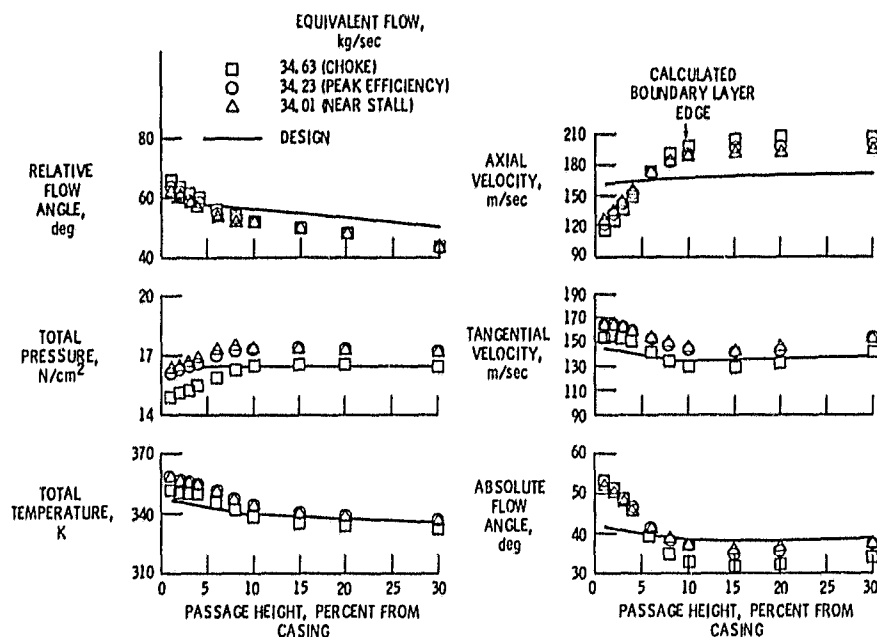


Figure 11. - Radial distributions at measuring station 2, first-stage rotor exit.

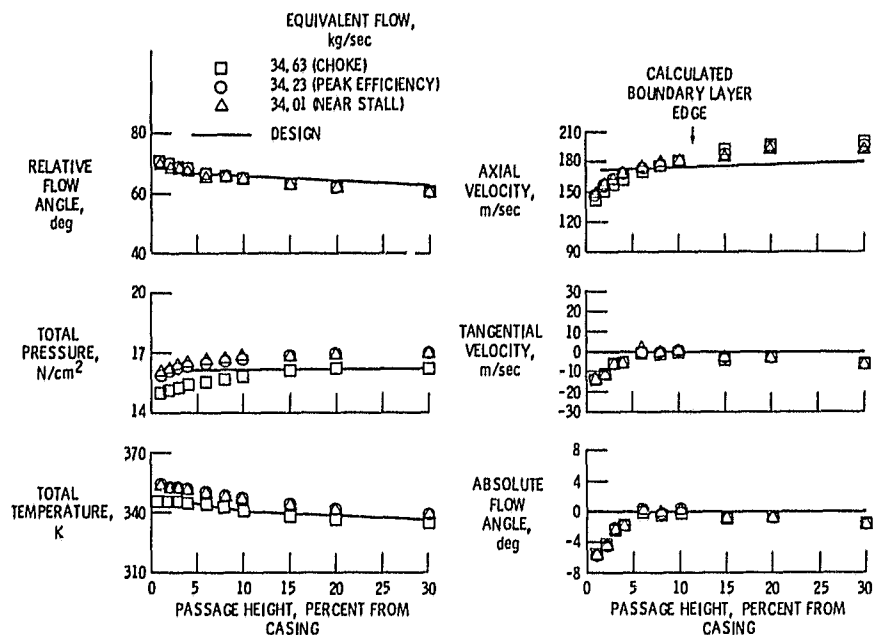


Figure 12. - Radial distributions at measuring station 3, first-stage stator exit.

ORIGINAL PAGE IS
OF POOR QUALITY

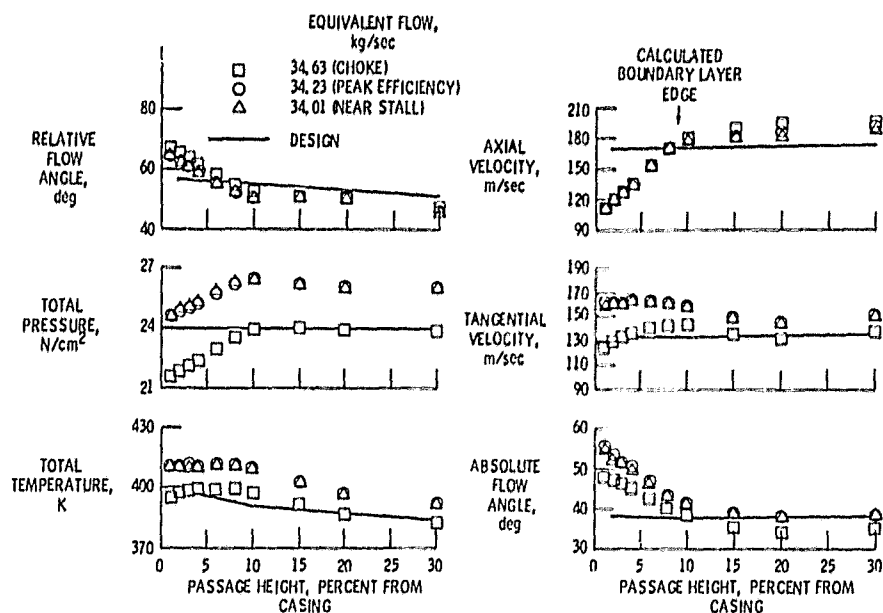


Figure 13. - Radial distributions at measuring station 4, second-stage rotor exit.

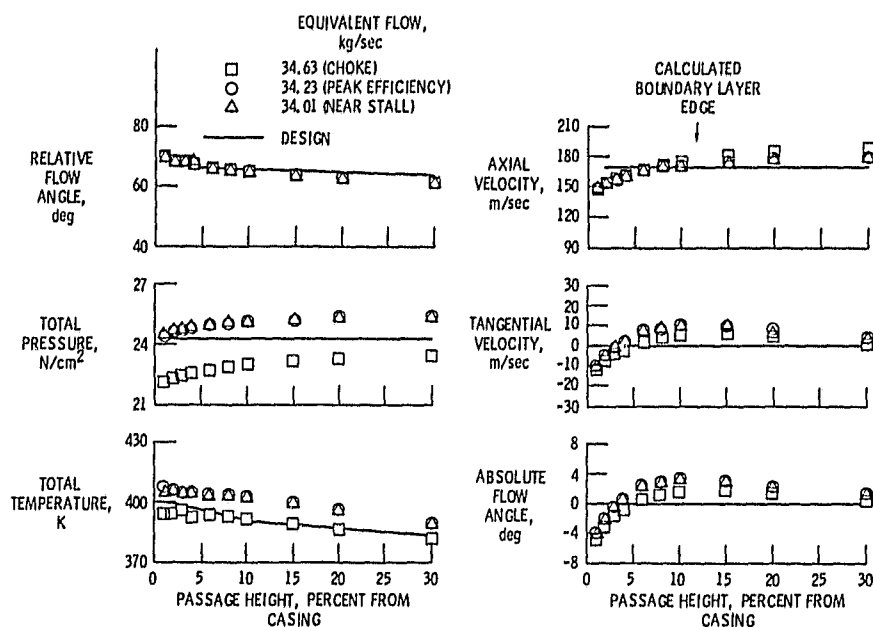


Figure 14. - Radial distributions at measuring station 5, second-stage stator exit.

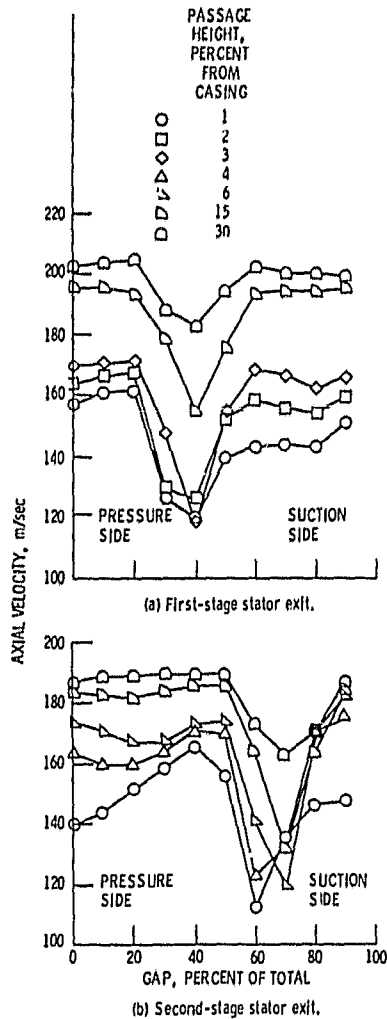


Figure 15. - Circumferential variation of axial velocity at stator exits. Mass flow, 34.23 kg/sec.

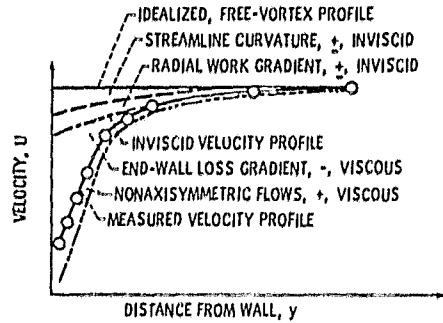


Figure 16. - Factors affecting measured velocity profiles.

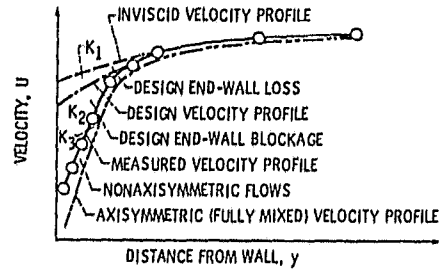


Figure 17. - Comparison between design and measured blockage allowance. $K_{meas} = K_1 + K_2$, $K_{des} = K_2 + K_3$.

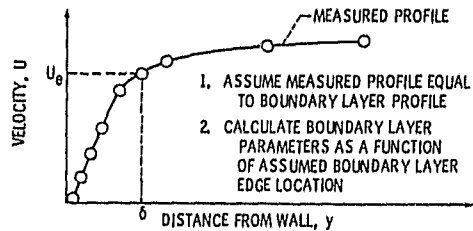


Figure 18. - Standard method of calculating boundary layer parameters from measured data.

ORIGINAL PAGE IS
OF POOR QUALITY

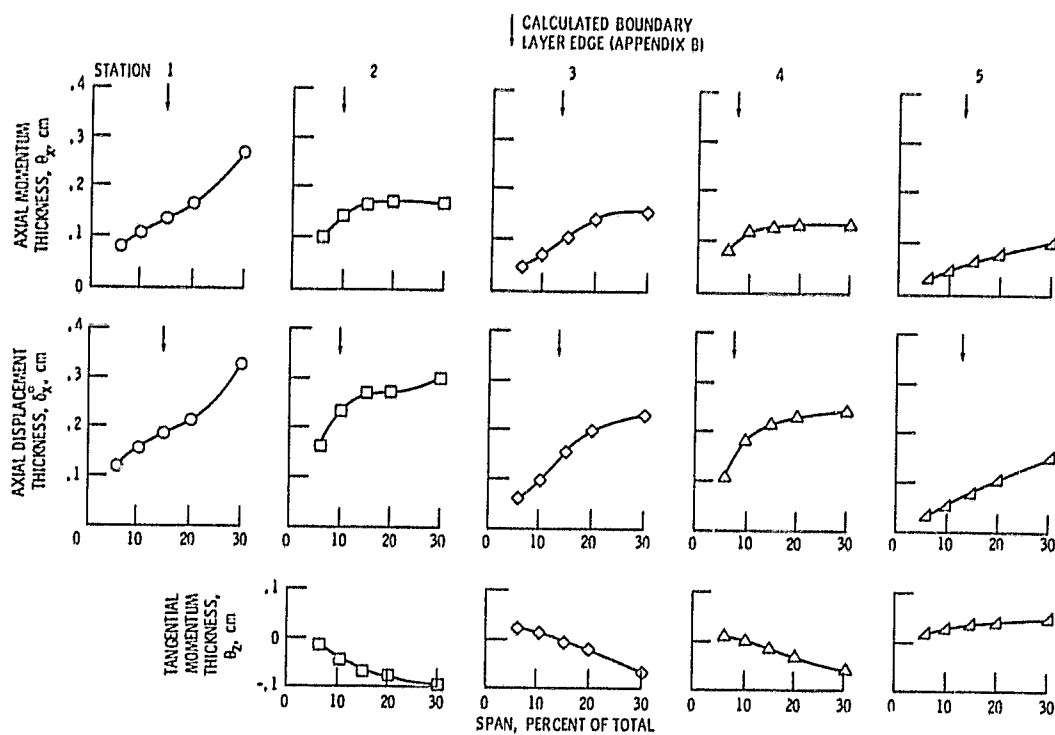


Figure 19. - Calculated boundary layer parameters from measured velocity profiles.